Article

Mapping the Morphology of DNA on Carbon Nanotubes in Solution Using X-ray Scattering Interferometry

Daniel J. Rosenberg, Francis J. Cunningham, Joshua D. Hubbard, Natalie S. Goh, Jeffrey Wei-Ting Wang, Shoichi Nishitani, Emily B. Hayman, Greg L. Hura, Markita P. Landry, and Rebecca L. Pinals*

Read Online

ACCESS | 📊 Metrics & More | 📖 Article Recommendations | 🆂🅸 Supporting Information

ABSTRACT: Single-walled carbon nanotubes (SWCNTs) with adsorbed single-stranded DNA (ssDNA) are applied as sensors to investigate biological systems, with potential applications ranging from clinical diagnostics to agricultural biotechnology. Unique ssDNA sequences render SWCNTs selectively responsive to target analytes such as $(GT)_n$-SWCNTs recognizing the neuromodulator, dopamine. It remains unclear how the ssDNA conformation on the SWCNT surface contributes to functionality, as observations have been limited to computational models or experiments under dehydrated conditions that differ substantially from the aqueous biological environments in which the nanosensors are applied. We demonstrate a direct mode of measuring in-solution ssDNA geometries on SWCNTs via X-ray scattering interferometry (XSI), which leverages the interference pattern produced by AuNP tags conjugated to ssDNA on the SWCNT surface. We employ XSI to quantify distinct surface-adsorbed morphologies for two $(GT)_n$ ssDNA oligomer lengths ($n = 6, 15$) that are used on SWCNTs in the context of dopamine sensing and measure the ssDNA conformational changes as a function of ionic strength and during dopamine interaction. We show that the shorter oligomer, $(GT)_6$, adopts a more periodically ordered ring structure along the SWCNT axis (inter-ssDNA distance of 8.6 ± 0.3 nm), compared to the longer $(GT)_{15}$ oligomer (most probable 5′-to-5′ distance of 14.3 ± 1.1 nm). During molecular recognition, XSI reveals that dopamine elicits simultaneous axial elongation and radial constriction of adsorbed ssDNA on the SWCNT surface. Our approach using XSI to probe solution-phase morphologies of polymer-functionalized SWCNTs can be applied to yield insights into sensing mechanisms and inform future design strategies for nanoparticle-based sensors.
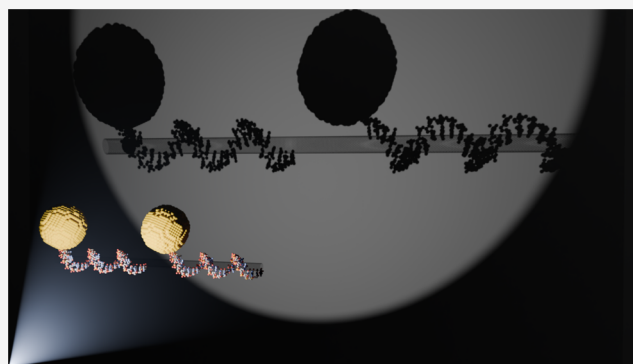
INTRODUCTION

Single-walled carbon nanotubes (SWCNTs) serve as tools for biological sensing, imaging, and delivery applications.[1,2] SWCNTs are an advantageous platform due to their sensitive fluorescence response to localized changes (motivating sensor development[3−5]), photostable near-infrared fluorescence in the tissue-transparency window (enabling *in vivo* imaging[6,7]), and nanometer-sized diameter with a high aspect ratio (supporting use as cell-permeable delivery vehicles[8−10]). For each of these respective applications, the nanotube surface acts as a substrate upon which sensing moieties, antibiofouling ligands, or delivery cargoes are loaded. Specifically, SWCNTs with adsorbed nucleic acids have been applied as nanoparticle-based sensors and delivery agents. Polymer properties, including nucleic acid sequence and length, govern SWCNT-adsorbed morphology, stability, and function. These constructs have proven particularly useful as nanosensors for small-molecule analytes including catecholamines,[11−14] serotonin,[15,16] hydrogen peroxide,[17−19] and nitric oxide.[20,21]

Despite over a decade of development in SWCNT-based sensors, there remain contrasting theories about what enables molecular recognition and what role conformational shifts may play. For example, a particular sequence of single-stranded DNA (ssDNA)—a repeating motif of guanine and thymine (GT)—has enabled highly sensitive and spatially resolved dopamine detection from single neurons *in vitro* and in brain slice culture.[11−14] Hypothesized interaction mechanisms between the dopamine and GT oligomer include dual hydrogen bonding between the two hydroxyl groups of dopamine and the phosphate backbone of the ssDNA,[12] a redox reaction,[3] and/or intercalation of the aromatic catechol-amine ring between the ssDNA oligomer and SWCNT surface
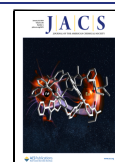
driven by $\pi-\pi$ stacking.[3] Optimizing interactions of nucleic acids with SWCNTs is key to the success of these biotechnologies, yet challenges remain in directly measuring, in real time, how ssDNA-SWCNT sensors function.

Current methods for characterizing ssDNA-SWCNT conformations involve a dehydrated sample immobilized on a two-dimensional substrate, despite SWCNT-based biotechnologies mainly being applied in the aqueous solution state. Such characterization techniques include transmission electron microscopy (TEM) to visualize ssDNA-SWCNT morphology[22,23] and atomic force microscopy (AFM) to determine dimensions and packing of biomolecules on SWCNTs,[8,24−27] which has been previously demonstrated to suffer from adsorption biases introduced during sample preparation.[28] Other physical properties such as hydrodynamic dimensions can potentially be extracted from dynamic light scattering (DLS) measurements on SWCNTs performed in the solution state. However, rigorous optical scattering methods have not been well-adapted for nonspherical, high-aspect-ratio particles such as SWCNTs and cannot resolve fine-grained surface features such as nanometer-scale polymer packing.

Small-angle X-ray scattering (SAXS) has shown promise in revealing the morphology of SWCNT-based systems in solution.[29,30] We have previously reported the use of SAXS to determine the in-solution structure of ssDNA-suspended SWCNTs interacting with blood plasma proteins.[31] Yet, SAXS is a contrast measurement technique relying on the scattering intensity of the analyte (proportional to the square of the electron density) being significantly higher than that of the solution. Thus, materials of relatively low electron density such as carbon-based SWCNTs and ssDNA must be at sufficiently high concentrations for the signal to be above background. Accordingly, characterizing ssDNA-SWCNTs via SAXS requires the use of SWCNT concentrations that exceed those applied in biological systems (0.1−5 mg/L).[1,11,32] Elevated concentrations can lead to artifacts such as intertube bundling of the ssDNA-SWCNTs,[23,29] which must be minimized to fully elucidate the morphology of individual ssDNA-functionalized SWCNT sensors. A strategy to overcome this concentration issue for low-scattering materials is to increase the X-ray exposure time, but this risks creating chemical changes in solution that can affect the sample under study.[33] An alternative approach is to directly increase the electron density of the sample using high-contrast materials such as gold nanoparticles (AuNPs) and then apply X-ray scattering interferometry (XSI), originally described by Mathew-Fenn et al.[34,35] XSI leverages the interference patterns generated by X-ray scattering between ordered AuNPs to measure discrete inter-AuNP distances, effectively turning the AuNPs into molecular rulers in solution.[34−40] Additionally, through adaptation of robotics and a rapid data-processing pipeline, XSI can be run at higher throughput with minimal sample consumption (averaging one sample per minute, with ≤30 μL volume per sample).[40−42]

Herein, we apply XSI to investigate the nanopatterning of the adsorbed ssDNA corona surrounding the SWCNT in the solution phase. Small AuNPs are attached to the 5′ end of each ssDNA oligomer and purified to ensure one AuNP tag per ssDNA strand,[39,40] and the ssDNA-AuNPs are adsorbed to the SWCNT surface to form a ssDNA-AuNP-SWCNT complex. We focus on an illustrative example of how surface-constrained polymer conformation influences sensor properties by studying two $(GT)_n$ ssDNA sequences (n = 6 and 15) used for

dopamine sensing. These two ssDNA oligomers empirically possess different advantageous properties, with $(GT)_6$ displaying a larger magnitude of fluorescence change in response to dopamine[43] and $(GT)_{15}$ displaying higher stability in relevant biomolecule-rich environments.[44] Previous characterization by experimental studies (AFM, EM)[22,24] and molecular dynamics (MD) simulations[43] suggests that these two oligomers possess distinct surface-constrained conformations: the shorter $(GT)_6$ oligomer is expected to form a ring-like structure around the nanotube and the longer $(GT)_{15}$ oligomer is expected to form a helical wrapping around the nanotube. We employ high-throughput XSI in solution at biologically applicable concentrations to explore: (i) the configuration of adsorbed ssDNA along the SWCNT surface, (ii) the conformational changes of adsorbed ssDNA as a function of ionic strength, and (iii) the behavior of adsorbed ssDNA in the presence of the target analyte, dopamine. Additionally, we perform *ab initio* modeling of the AuNPs on the SWCNT surface directly from scattering profiles to provide a more comprehensive three-dimensional (3D) view of the system. We validate our technique with other suspension characterization (absorbance, fluorescence, DLS, TEM). Taken together, this approach establishes a high-throughput technique for in-solution characterization of nanotube-based biotechnologies, with promise for extension to other nanoparticle substrates, and provides a deeper understanding of the mechanisms behind their molecular recognition of analytes.

■ RESULTS AND DISCUSSION

Synthesis and Characterization of ssDNA-AuNP-SWCNTs. To first demonstrate the resolvable concentration range for ssDNA alone and ssDNA-SWCNTs without AuNP tags, we collected SAXS profiles of serial dilutions for $(GT)_{15}$ ssDNA and $(GT)_{15}$-SWCNTs (Figure S1A,B). No usable scattering profiles were obtained at concentrations below 62.5 μM from ssDNA alone. Bundled ssDNA-SWCNTs were observed even at the lowest resolvable concentration of 16 mg/L, with average bundling of an estimated 6−8 SWCNTs obtained from the cross-sectional radius of gyration. These results and electron density calculations (see the Methods Section and Supporting Information, Section S.1) motivate our use of small AuNP tags to increase the electron density of our material and thus observe ssDNA-SWCNTs in solution at relevant applied concentrations (≤5 mg/L ssDNA-SWCNTs). Citrate-capped AuNPs were synthesized, conjugated to ssDNA via trithiolated linkers (Letsinger's type) on the 5′ end, and coated with methoxy poly(ethylene glycol) thiol (mPEG-SH) as detailed in the Methods Section. Monoconjugated ssDNA-AuNPs (5.9−7.2 nm diameter) were fractionated by anion-exchange chromatography (Figure S2), characterized by SAXS to determine morphology and polydispersity (Figure S3A−C and Tables S1 and S2), and characterized by DLS to determine hydrodynamic radius (Figure S3D and Table S3). Absolute-scale intensity scattering measurements demonstrate that scattering from 6.9 nm diameter PEGylated AuNPs (PEG-AuNPs) is approximately 65,000-fold higher than that of $(GT)_{15}$ ssDNA and approximately 270-fold higher than that of $(GT)_{15}$-SWCNTs (Figure S1C) at the same relative concentrations (250 nM AuNP and ssDNA per 1 mg/L SWCNT). The measured scattering in the conjugated ssDNA-AuNP-SWCNTs is thus dominated by the AuNP signal and eliminates the need to mathematically factor in the scattering contributions from the ssDNA or SWCNT alone or the
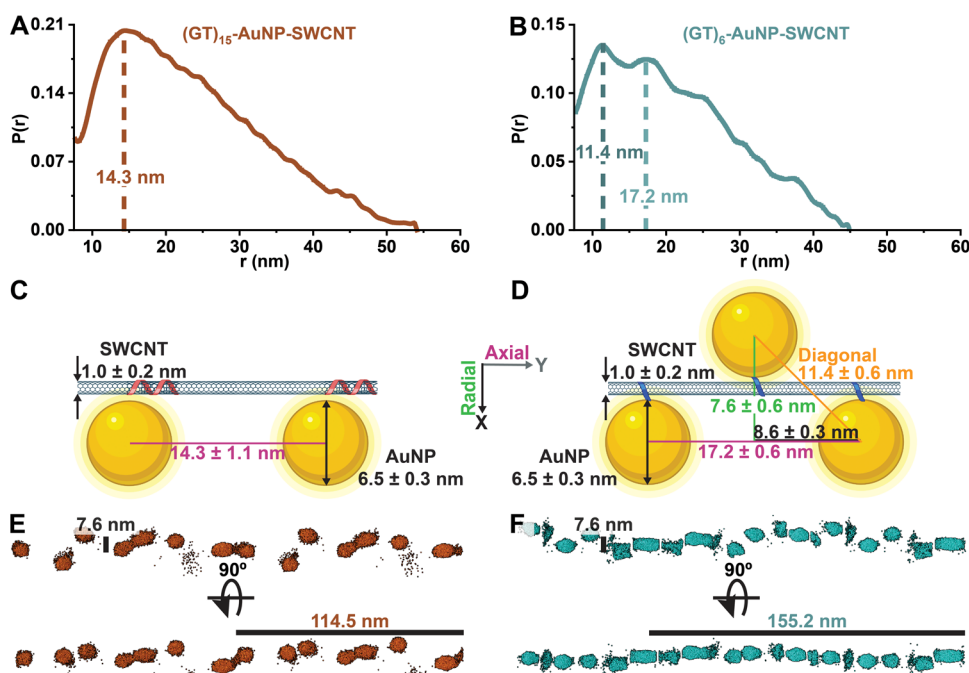
Figure 1. ssDNA forms ordered structures on the carbon nanotube surface in solution. (A, B) Pairwise distribution functions, $P(r)$, from XSI data reveal discrete distances of AuNP-tagged ssDNA along the nanotube surface for (A) $(GT)_{15}$-AuNP-SWCNTs and (B) $(GT)_6$-AuNP-SWCNTs. $P(r)$ functions are normalized to the primary intra-AuNP peak, then the x-axis minimum is set to focus on the inter-AuNP peak for clarity. (C, D) 2D schematics for proposed geometric arrangements of AuNPs on SWCNTs, with average inter-AuNP distances obtained from statistical analysis of $P(r)$ functions for (C) $(GT)_{15}$-AuNP-SWCNTs and (D) $(GT)_6$-AuNP-SWCNTs. Average inter-AuNP distances are denoted as diagonal (orange), axial (magenta), and radial (green). Schematics are drawn close to scale and show the most probable distances rather than a distribution for clarity. The $(GT)_{15}$ polymer footprint in panel (C) is drawn based on a 2 nm helical pitch leading to 4 nm total footprint length as calculated from MD simulations.[43] (E, F) *Ab initio* modeling results for (E) $(GT)_{15}$-AuNP-SWCNTs and (F) $(GT)_6$-AuNP-SWCNTs. These models represent the calculated arrangement of AuNPs (shown as regions of high atomic density) on the SWCNT surface (not shown), with a 90 rotation along the SWCNT axis included in the second row. Fits and residuals are included in Figure S14.

scattering cross-terms between the different components of the complex.

We apply XSI to study two ssDNA sequences based on their relevance to biomolecular sensing and predicted surface-adsorbed conformational differences: $(GT)_{15}$ and $(GT)_6$.[11,12,22,43] SWCNTs were suspended with monoconjugated ssDNA-AuNPs by probe-tip sonication at a constant ssDNA:SWCNT ratio (250 nmol ssDNA-AuNP per 1 mg SWCNT), in line with previous literature.[11,45] We optimized this suspension method with the added AuNP tag by screening alternative approaches and lowering the net concentration, as detailed in the Methods Section and Supporting Information, Section S.2. The absorbance and fluorescence of the resulting suspensions were characterized to corroborate the formation of ssDNA-AuNP-SWCNT complexes (Figure S4). Retention of the AuNP plasmon resonance peak at approximately 520 nm reveals that the AuNP tags remain intact and well-dispersed through the SWCNT complexation process (Figure S4A). Absorbance peaks in the near-infrared region associated with the SWCNTs are not resolvable at this low suspension concentration (approximately 0.2 mg/L SWCNTs); therefore, the x-axis range is adjusted for clarity. Fluorescence spectra for AuNPs alone (with or without ssDNA) at 721 nm laser excitation reveal a trough in the emission intensity centered at approximately 950 nm. This optical feature may be due to absorption of excitation light, despite the lack of a distinct absorption band at this location. The SWCNTs used in this study are of mixed chirality, with excitation at 721 nm producing the highest intensity emission peak at approximately

1125 nm indicative of contributions from the dominant chiralities of (9,4) SWCNTs and off-resonance excitation of (8,4), and (7,6) SWCNTs, with diameters of 0.916, 0.840, and 0.895 nm, respectively.[46] Compared to the fluorescence spectrum of the ssDNA-SWCNTs alone, addition of the AuNP tags results in lower intensity and broadened SWCNT fluorescence emission peaks in the near-infrared region, with more prominent emission peaks retained at longer wavelengths (Figure S4B−D). This peak-broadening effect that the AuNPs impart on the SWCNT fluorescence may indicate a lower suspension yield and/or electronic/excitonic interaction, underscoring the proximity of AuNPs to the SWCNT surface because SWCNTs are highly sensitive to perturbations in their local dielectric environment. The retention of fluorescence at longer wavelength peaks suggests that more large-diameter SWCNTS are individually dispersed with the ssDNA-AuNPs, but this effect is convoluted by the trough introduced by the AuNPs at approximately 950 nm.

Conformational Geometries of ssDNA on SWCNTs from XSI. The ssDNA-AuNP-SWCNT complexes were next analyzed by XSI. This technique is an extension of traditional solution SAXS in which a radial average of X-rays scattering off the electron density of a sample is integrated, and the contrast between the sample and buffer is used to produce a buffer-subtracted one-dimensional (1D) curve in reciprocal space. The total scattering intensity is the summation of two terms: the form factor, arising from the particle size and morphology, and the structure factor, derived from interparticle interactions. For SAXS measurements of biomolecules in solution, the

sample conditions (*e.g.*, concentration) are adjusted to experimentally remove contributions of the structure factor to isolate the form factor. An inverse Fourier transform of the subtracted curves then produces a pairwise distribution function ($P(r)$; a probability plot of all interelectron distances), providing real-space information on the average shape of the electron density of individual macromolecules free from interparticle interaction.[47,48] Conversely, in XSI, the structure factor is of primary importance and represents the interference pattern of scattered X-rays arising from inter-AuNP interactions, specifying discrete distances between ordered AuNPs.[35,39,40] Thus, we base our findings primarily on the structure factor contributions to the overall scattering profile but choose to retain the form factor for purposes of normalization to account for slight fluctuations in sample concentration and X-ray beam intensity. Additionally, including the intragold contribution to the scattering provides an internal standard for the individual AuNPs, allowing analysis of particle size and polydispersity that aids in geometric calculations of ssDNA-AuNPs adsorbed to the SWCNT surface. For the mathematical fundamentals of SAXS, readers are encouraged to refer to the quintessential work by Putnam et al.[47]

We measured ssDNA spacing along SWCNTs using the AuNP tags via XSI (Figure 1A−B, with details in the Methods Section). Real-space analysis of the $P(r)$ functions shows two main peak regions (Figure S5). The first peak represents the intra-AuNP distances between electrons within individual AuNPs, with the peak maximum being the average radius of the AuNP. The absence of additional peaks in the $P(r)$ functions without SWCNTs indicates that there is no long-range order and that the ssDNA-AuNPs are free in solution. For clarity, the intra-AuNP peak is omitted in the main text figures but is included in Supporting Information figures. The subsequent peaks in the $P(r)$ functions represent the probability distribution of inter-AuNP distances and is only observed in complexes containing periodic ordering of AuNPs. Though these structures must have a degree of order to show discrete inter-AuNP distances, XSI is a bulk technique in solution and thus requires statistical analysis across multiple samples with multiple scans to obtain useful geometric values. Statistical analysis of the most prominent peaks and shoulders of this broader distribution reveals the distinct surface-adsorbed spacings of $(GT)_{15}$- and $(GT)_6$-AuNPs on the nanotube surface (Figure 1A,B). Importantly, ssDNA-AuNPs (without SWCNT substrates) are in a disordered state when free in solution and enter a periodically ordered state only when adsorbed to the SWCNT surface (Figures S5 and S6). TEM visualization recapitulates these findings in the dried state, showing ssDNA-AuNPs adsorbed to SWCNTs (Figures S7 and S8) or disordered and free in the absence of SWCNTs (Figure S9; see full image analysis details in Supporting Information, Section S.3 and Figure S10).

A series of controls was conducted to confirm that the preparation of ssDNA-AuNP-SWCNT complexes leads to adsorption of ssDNA-AuNPs on the SWCNT surface rather than an off-target aggregative process: there is no inter-AuNP contribution to the scattering profiles in the case of ssDNA-SWCNTs (no AuNPs), free ssDNA-AuNPs (no SWCNTs), carboxylated SWCNTs mixed with ssDNA-AuNPs (no probe-tip sonication and thus no driving force for self-assembly), and SWCNTs attempted-to-be suspended with PEG-AuNPs (no ssDNA) (Figure S11). Additionally, there is no ssDNA-AuNP-

SWCNT concentration dependence over the range used in this study (0.17−1.76 mg/L; Figure S12), which is within the unbundled SWCNT regime based on a previous study.[23] Finally, there is no AuNP size dependence for the axial inter-AuNP distances over the range used in this study (5.9−7.2 nm diameter; Figure S13A−C). While the packing of ssDNA on the SWCNT surface is unchanged by potential steric effects from the AuNPs within this diameter range of 1.3 nm, this does not preclude the possibility that the AuNPs affect the ssDNA conformation and dynamics, as will be explored further.

MD simulations have predicted that $(GT)_{15}$ forms a helical wrapping around SWCNTs with uniform electrostatic potential profiles averaged across the helix, as opposed to the ring-like conformation of $(GT)_6$ showing a periodic electrostatic footprint of alternating positive and negative surface potentials.[43] From XSI, the generally broader and less spatially resolved inter-AuNP peaks observed for $(GT)_{15}$-AuNP-SWCNTs suggest a more variable surface adsorption pattern (Figures 1A and S7). Due to this increased variability in $(GT)_{15}$-AuNP adsorption and lack of orientational reference, a statistical analysis of the most probable inter-AuNP distances (14.3 ± 1.1 nm; replicates $n \geq 14$) is used to determine the basic 1D axial ssDNA spacing along the SWCNT (Figures 1C and S13A,C). This most probable inter-AuNP distance based on XSI is higher than the average axial inter-AuNP distance estimated from TEM (9.8 ± 5.1 nm; see details in Section S.3), suggesting that the inter-AuNP distance is not at the upper packing limit allowable by the size of AuNPs and that there is polymer compression upon dehydration for TEM. In contrast, the inter-AuNP peaks for $(GT)_6$-AuNP-SWCNTs are narrower and contain more clearly defined higher-order features after the initial, most probable separation distance (11.4 ± 0.6 nm; replicates $n \geq 16$; Figures 1B and S13B,C). MD simulations of $(GT)_6$ on (9,4) chirality SWCNTs (0.916 nm diameter) predict that there is a near-equivalent split in energetically favorable left-handed helix and ring-like conformations for a single ssDNA on the SWCNT surface, and that steric effects from multiple ssDNAs result in a population shift to primarily rings.[43] Accordingly, $(GT)_6$ is expected to adopt a ring-like configuration on the majority of SWCNTs used in this study (mixed chiralities, with an average diameter of 1 ± 0.2 nm).

From the longer-range distance features of the inter-AuNP peaks for $(GT)_6$-AuNP-SWCNTs, we deduce that the AuNPs align on alternating sides of the SWCNT. Specifically, the second-most probable inter-AuNP distance reveals an average center-to-center distance of 17.2 ± 0.6 nm (replicates $n \geq 16$; Figures 1B and S13B,C). Based on a simple geometric model, we hypothesize that this represents the inter-AuNP spacing axially down the SWCNT and the preceding peak at 11.4 nm is the distance of AuNPs diagonally across the SWCNT (Figure 1D). These inter-AuNP distances result in an average periodic inter-ssDNA ring distance of 8.6 ± 0.3 nm (Figure 1D). Notably, the average axial inter-AuNP distance from XSI (17.2 ± 0.6 nm) is over twice the axial inter-AuNP distance estimated from TEM (8.5 ± 3.1 nm; see details in Supporting Information, Section S.3), measured as center-to-center inter-AuNP distances of nearest neighbors on separate sides of the SWCNT. This difference and the remarkable similarity in the TEM-derived axial inter-AuNP distance histograms between $(GT)_{15}$- and $(GT)_6$-AuNP-SWCNTs below ∼12 nm (Figure S10B) strongly suggest that the inter-AuNP distance is dramatically changed upon dehydration during TEM prepara-
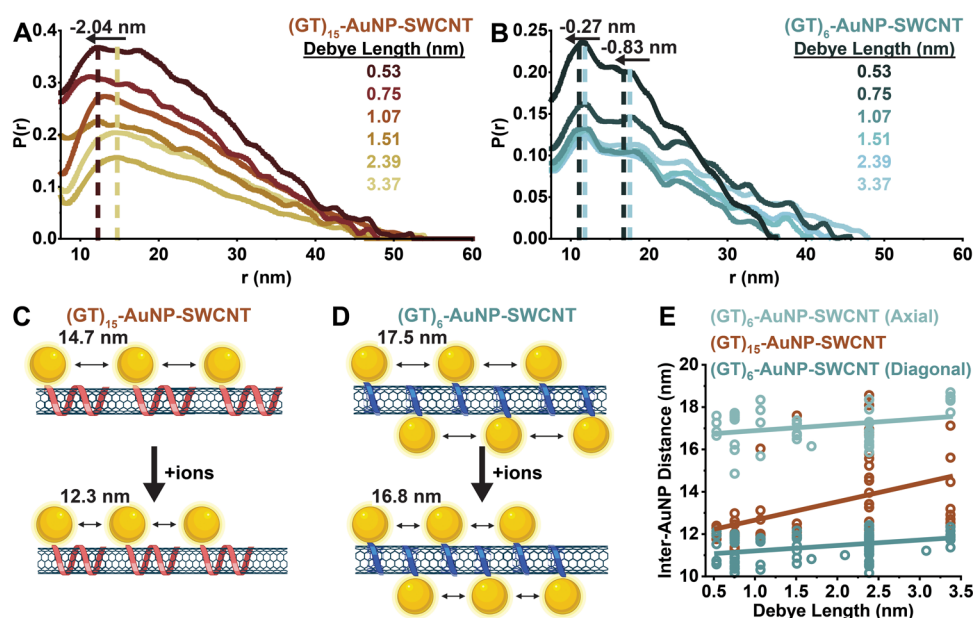
Figure 2. ssDNA spacing along the SWCNT surface is modulated as a function of the ionic strength. Representative pairwise distribution functions, $P(r)$, for (A) $(GT)_{15}$-AuNP-SWCNTs (red−orange series) and (B) $(GT)_6$-AuNP-SWCNTs (blue series) in phosphate-buffered saline of varying net salt concentration, as represented by Debye lengths (λ_D = 3.37−0.53 nm). Additional, representative $P(r)$ functions and scattering curves are included in Figures S5 and S6 for $(GT)_{15}$- and $(GT)_6$-AuNP-SWCNTs ($n \geq 4$ replicates per sample). Dashed vertical lines are added to visualize peak shifts, proceeding from light to dark dashed lines with an increase in ionic strength. $P(r)$ functions are normalized to the primary intra-AuNP peak, then the x-axis minimum is set to focus on the inter-AuNP peak for clarity. (C, D) Schematic representations of changes in inter-AuNP distances at elevated ion concentrations for (C) $(GT)_{15}$-AuNP-SWCNTs and (D) $(GT)_6$-AuNP-SWCNTs. Schematics are not drawn to scale. (E) Summary of inter-AuNP distances as a function of the Debye length for individual samples (dots) with the corresponding linear regression (lines). Replicates for each salt condition are $n \geq 4$.

tion. As expected, the axial inter-AuNP distances for both $(GT)_{15}$- and $(GT)_6$-AuNP-SWCNTs are not affected by changes in AuNP diameter because this is a center-to-center distance measurement (Figure S13C). Conversely, the diagonal distance is expected to change slightly as a function of the AuNP diameter, as calculated in Figure S13C when the AuNPs are flush with the SWCNT surface, holding to a two-dimensional (2D) geometry (deemed adequate due to the diameter disparity between AuNPs and SWCNTs). This trend is not seen experimentally, however, suggesting that the AuNPs are not directly in contact with the SWCNT surface, and their positional variance may preclude our ability to see this trend. To explore this positional variance, diagonal and axial inter-AuNP distances from a single size of AuNPs (d = 6.1 ± 0.03 nm) were used to calculate an average radial distance of 7.6 ± 0.6 nm (Figure S13D), indicating that the average distance from the SWCNT surface to the nanoparticle surface is 0.8 ± 0.3 nm.

We expand upon these simplified 2D geometric analyses with 3D visualization of the ssDNA-AuNPs adsorbed on the SWCNT surface through *ab initio* modeling directly from scattering profiles using SASHEL (see the Methods Section and Supporting Information, Section S.4). The final best-fit models demonstrate the complexity of these systems and validate our 2D interpretation (Figures 1E,F and S14A−C). *Ab initio* models for $(GT)_6$-AuNP-SWCNTs show increased AuNP packing density and greater consistency in inter-AuNP distances than $(GT)_{15}$-AuNP-SWCNTs. When rotated about the SWCNT axis, $(GT)_6$-AuNP-SWCNTs reveal a plane where there is little radial variance between AuNPs (Figure 1F), confirming our hypothesis that the small diameter of the SWCNT would reasonably support a 2D estimate of

geometries. Conversely, no such plane was found for the $(GT)_{15}$-AuNP-SWCNT models (Figure 1E).

Our calculated separation distances of ssDNA polymers along the SWCNT axis are in relative agreement with previous literature, though with the caveat that prior work has simulated non-AuNP-conjugated ssDNA on single-chirality SWCNTs or measured in the dehydrated state. Based on prior MD simulations, a single $(GT)_{15}$ polymer on a (9,4) chirality SWCNT is expected to extend approximately 4 nm in footprint length with an estimated 2 nm helical pitch (*i.e.*, each polymer wraps around the SWCNT twice), and $(GT)_6$ rings demonstrate periodic electrostatic potentials of approximately 1.5 nm in the footprint length.[43] Another MD simulation study similarly estimates the pitch of $(GT)_{30}$ oligonucleotides on (11,0) SWCNTs to be 2−8 nm, depending on the DNA backbone orientation (with the 8 nm pitch orientation more energetically favorable, albeit on larger-diameter SWCNTs).[49] DNA pitch on SWCNTs has also been visualized by TEM, with estimates of 2.2 nm pitch for double-stranded salmon testes DNA along SWCNTs.[50] Assuming that adjacent ssDNA strands are close but not intertwined along the SWCNT axis,[24] we calculate that the theoretical axial footprint for $(GT)_{15}$ ssDNA could range from 5.6 to 20.3 nm (2.8−1 turns of the helix around the SWCNT) and $(GT)_6$ ssDNA from 2.3 to 8.1 nm (1.1−1 turns of the ring around the SWCNT) (see Supporting Information, Section S.5). The directly measured 5′-to-5′ ssDNA spacings in solution of 14.3 ± 1.1 nm and 8.6 ± 0.3 nm for $(GT)_{15}$- and $(GT)_6$-AuNP-SWCNT, respectively, are therefore reasonable in comparison to those computationally predicted or measured in previous studies.[51,52]

Surface-Adsorbed ssDNA Structural Changes as a Function of Ionic Strength. We applied this XSI approach
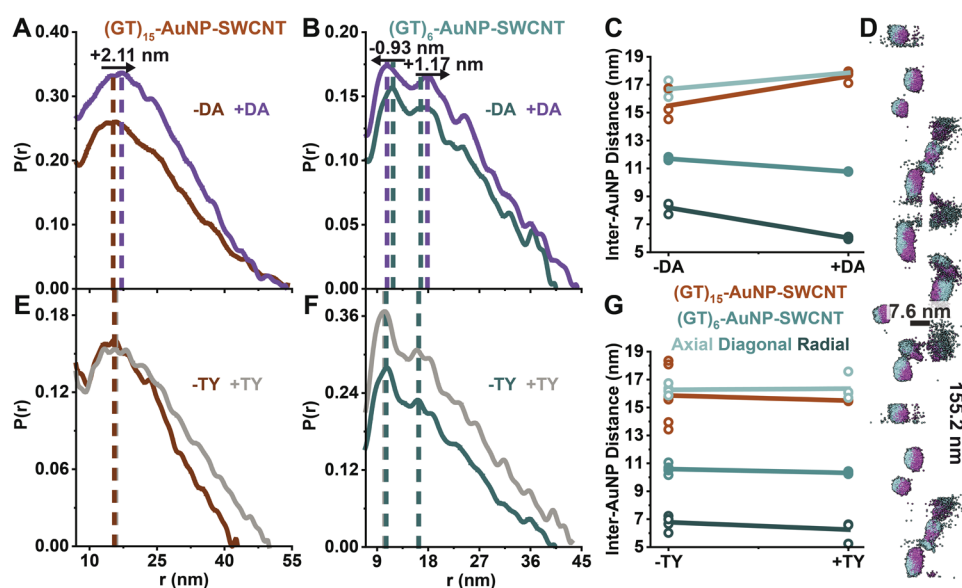
Figure 3. Dopamine interaction drives the axial lengthening and radial tightening of ssDNA on SWCNTs. Inter-AuNP spacings change in the presence of (A−D) dopamine (DA) but are absent with (E−G) p-tyramine (TY), a structural analogue and negative control. Representative pairwise distribution functions, $P(r)$, for (A, E) $(GT)_{15}$-AuNP-SWCNTs (red) and (B, F) $(GT)_6$-AuNP-SWCNTs (blue) with no analyte vs in the presence of (A, B) DA (purple) or (E, F) TY (gray). Dashed vertical lines are added to visualize peak shifts. $P(r)$ functions are normalized to the primary intra-AuNP peak, then the x-axis minimum is set to focus on the inter-AuNP peak for clarity. (C, G) Summary of inter-AuNP distances for replicates without and with (C) DA and (G) TY. Inter-AuNP distances are shown for individual samples (dots) with corresponding linear regressions (lines). $P(r)$ functions for replicates are shown in Figure S15 ($n \geq 3$ for each sample−analyte combination). (D) Ab initio modeling of $(GT)_6$-AuNP-SWCNTs recapitulates the decrease in radial inter-AuNP distances as the AuNPs move from the initial (blue) to the final state in the presence of DA (purple). Fit and residuals are shown in Figure S16.

to determine in situ ssDNA packing on the SWCNT surface as a function of the solution ionic strength (Figure 2). Increasing solution ionic strength is expected to modify the surface-adsorbed ssDNA conformation and thus AuNP scattering periodicity by screening the negatively charged phosphate backbone of the ssDNA and enabling closer packing along the nanotube surface.[53,54] To test this hypothesis, ssDNA-AuNP-SWCNTs were synthesized, dialyzed against 0.1X PBS, and then diluted to various PBS concentrations to achieve different net salt concentrations while maintaining constant pH. We tested samples in a range of 0.05× to 2× PBS represented as corresponding Debye lengths (λ_D) ranging from 3.37 to 0.53 nm, calculated as previously described.[55] This range was selected because ssDNA-SWCNTs are unstable against bundling in pure water, and PBS concentrations above 2× resulted in aggregation.

As predicted, the longer, multipass helices of $(GT)_{15}$ on the nanotube surface compress at increased salt conditions (lower λ_D) from inter-AuNP distances of 14.7 to 12.3 nm (Figure 2A,C,E). However, the spacing of the shorter, single-pass rings of $(GT)_6$ did not change as significantly with the ionic strength in either diagonal or axial inter-AuNP distances (Figure 2B,D,E). An axial inter-AuNP shift from 17.5 to 16.8 nm was measured, corresponding to inter-ssDNA distances of 8.8 to 8.4 nm (for λ_D of 3.37 vs 0.53 nm). The calculated radial distances show negligible changes as a function of ionic concentration (Figure S13D). Given the smaller decrease in inter-AuNP distance observed for $(GT)_6$-AuNP-SWCNT at increased ionic strengths compared to that of $(GT)_{15}$-AuNP-SWCNT, we postulate that the high-salt condition affects the local intrastrand pitch to a greater extent than the neighboring interstrand interactions. This phenomenon may arise because the charged phosphate backbones on an ssDNA strand are in

closer proximity to each other than those on neighboring strands, and thus, ionic strength has a greater effect on the local electrostatic repulsion. Specifically, the range of Debye lengths probed in this experiment are closer to the order of intrastrand distances than interstrand distances. Moreover, increasing the concentration of ions in solution does not alter the radial distances of $(GT)_6$-AuNPs across the SWCNT, as expected due to the short-range nature of the $\pi-\pi$ interactions between the ssDNA and SWCNTs. Our salt-dependent ssDNA surface-packing results for $(GT)_{15}$ spacing on SWCNTs are in line with previous literature demonstrating this phenomenon with longer ssDNA on SWCNTs via indirect optical measurement and dried-state characterization:[53,54] at high salt concentrations, $(GT)_{30}$ adopts a more compact conformation with higher SWCNT surface coverage,[53] putatively due to self-stacking of nucleobases from a related MD study.[56] In comparison, the ssDNA enters an elongated and stiffer conformation at low salt concentration, accompanied by ssDNA desorption from the SWCNT reducing the packing density.[53]

ssDNA-SWCNT Nanosensor Interactions with Dopamine. We employed XSI to explore the ssDNA conformational changes of $(GT)_{15}$- and $(GT)_6$-AuNP-SWCNT complexes in the presence of the nanosensor target analyte, dopamine (DA) (Figure 3). Upon injection of 100 μM DA, a shift in the average inter-AuNP distances was observed in the $P(r)$ functions for both ssDNA oligomers. $(GT)_{15}$ strand spacing increased by 2.11 ± 1.0 nm (Figures 3A,C, and S15A), while the axial $(GT)_6$ strand spacing increased by only 0.59 ± 0.27 nm (as calculated from the axial inter-AuNP peak shift of 1.17 ± 0.55 nm) and the diagonal inter-AuNP peak revealed an average shift of −0.93 ± 0.11 nm (Figures 3B,C and S15B). Based on this observation, we calculated a corresponding radial

inter-AuNP distance shift of -2.27 ± 0.41 nm for $(GT)_6$-AuNP-SWCNTs in the presence of DA, reducing the average SWCNT-to-AuNP surface distance to -0.07 ± 0.04 nm. This decrease in the radial distance demonstrates that DA causes the ssDNA to move closer to the SWCNT surface, drawing in the AuNP tags. Moreover, this slightly negative SWCNT-to-AuNP distance may suggest that the AuNPs begin to overlap in the plane of the SWCNT, and thus, the ssDNA rings may be preferentially wrapping in opposite directions. This has not been previously observed experimentally or *in silico*, though may have been overlooked in prior analyses. Of note, this shortening of the radial inter-AuNP distances is not observed as a function of ionic strength (Figure S13D) and underscores the analyte-specific binding capabilities of this surface-constrained ssDNA sequence. *Ab initio* modeling of the AuNPs adsorbed on the SWCNT surface enables visualization of the decrease in the average radial inter-AuNP distances for $(GT)_6$-AuNP-SWCNTs in the presence of DA (Figures 3D and S16).

From the axial expansion of $(GT)_n$ down the length of the SWCNT and simultaneous radial constriction of $(GT)_6$ onto the SWCNT, we postulate that DA both interacts with the phosphate groups of the ssDNA and inserts between neighboring ssDNA strands, depending on the initial conformation of the adsorbed polymers (Figure S17). Previous MD simulations of (8,8) chirality $(GT)_{15}$-SWCNTs ($d = 1.1$ nm) in the presence of DA suggest that both the hydroxyl groups (protonated at pH 7.4) and amine groups of DA interact with the exposed phosphate groups of the ssDNA backbone, drawing the ssDNA closer to the SWCNT surface.[12] Another MD study of (9,4) chirality $(GT)_{15}$- and $(GT)_6$-SWCNTs ($d = 0.916$ nm) reports that the amine of DA interacts with the phosphate backbone by inserting between consecutive bases of the helically wrapped $(GT)_{15}$, but fails to insert between the bases of the ring-like $(GT)_6$, forming bridges between neighboring strands instead.[43] Both proposed mechanisms show that the DA interaction creates localized perturbations in the periodically ordered ssDNA-induced electrostatic surface potentials of the SWCNT. These perturbations modulate exciton recombination lifetimes and lead to a large increase in nanosensor fluorescence. Our observation that the axial distances of $(GT)_{15}$-AuNP-SWCNTs increase to a greater extent than $(GT)_6$-AuNP-SWCNTs complements the hypothesis that DA preferentially inserts between the bases for $(GT)_{15}$, increasing the pitch and hence footprint length along the SWCNT surface. Interestingly, as observed in $(GT)_6$-AuNP-SWCNTs, the presence of DA also constricts the ring-like structure around the SWCNT, suggesting that the DA interaction is pulling the phosphate backbone of ssDNA toward the SWCNT surface. This interaction may also be the case for $(GT)_{15}$-SWCNTs, but no radial distances can be calculated due to the lack of an orientational reference. As a control, XSI was collected for ssDNA-AuNP-SWCNTs in the presence of the dopamine analogue *p*-tyramine (TY), containing only one hydroxyl group. Negligible changes in the ssDNA distances were observed upon injection of TY (Figures 3E−G and S15C,D), consistent with the lack of fluorescence response and predictions from MD simulations.[11,43] We further demonstrate that the ssDNA-AuNP-SWCNTs are capable of a fluorescence response upon molecular recognition of DA, absent in the presence of TY (Figure S18).

CONCLUSIONS

In this work, we demonstrate that XSI is a valuable technique for studying $(GT)_n$-SWCNTs ($n = 6, 15$) in solution using small AuNP tags conjugated to the ssDNA to act as molecular rulers. XSI harnesses the tightly packed, electron-rich gold atoms in AuNPs to enable the study of structuring within nanomaterial assemblies at concentrations relevant to biological applications (0.1−5 mg/L). We find ordering of ssDNA-AuNPs along the SWCNT axis, with the most probable 5′-to-5′ ssDNA spacing of 14.3 ± 1.1 nm for $(GT)_{15}$ and inter-ssDNA spacing of 8.6 ± 0.3 nm for $(GT)_6$.

Exploration of *in situ* ssDNA packing on the SWCNT surface as a function of solution ionic strength over the range of 0.05× to 2× PBS ($\lambda_D = 3.37-0.53$ nm) reveals an inter-AuNP spacing decrease for $(GT)_{15}$-AuNP from 14.7 to 12.3 nm and $(GT)_6$-AuNP from 8.8 to 8.4 nm. These results reflect the predicted electrostatic charge screening of the ssDNA backbone to permit a closer packing. From these findings, we posit that the high-salt condition has a greater effect on the local intrastrand pitch (predominant for $(GT)_{15}$) rather than on the neighboring interstrand interactions (predominant for $(GT)_6$), leading to the larger change in inter-AuNP spacing in the former case. The minimal change in radial AuNP spacing as a function of solution ionic strength suggests a lesser role of electrostatics in driving ssDNA-SWCNT adsorptive interactions, as expected for the likely $\pi-\pi$ and hydrophobic forces governing polymer-surface adsorption.

XSI elucidates the conformational changes of $(GT)_{15}$ and $(GT)_6$ ssDNA adsorbed on SWCNTs in the presence of the nanosensor target analyte, dopamine. Upon dopamine addition, we postulate that the $(GT)_n$ ssDNA is perturbed by both axial ssDNA expansion and radial ssDNA constriction, leading to the increase in nanosensor fluorescence. In the presence of DA, the inter-AuNP distance increases by 2.11 ± 1.0 nm for $(GT)_{15}$-AuNPs and by only 0.59 ± 0.27 nm for $(GT)_6$-AuNPs. The greater shift in spacing for $(GT)_{15}$-AuNPs indicates that DA inserts between bases to a higher degree for the helically wrapped $(GT)_{15}$, increasing the pitch and hence the footprint length on the SWCNT surface as previously predicted.[43] Interestingly, for $(GT)_6$-AuNP-SWCNTs, the radial inter-AuNP distances show a decrease of 2.2 ± 0.41 nm in the presence of DA, which is not detected in response to changes in the salt concentrations. *Ab initio* modeling provides insight into a mechanism of $(GT)_6$ ring tightening, likely caused by the hydroxyl groups of DA interacting with the exposed phosphate groups of the ssDNA, pulling the ssDNA closer to the SWCNT surface. This constriction leads to a calculated SWCNT-to-AuNP surface distance of -0.07 ± 0.04 nm, implying that AuNPs may overlap in the plane on one side of the SWCNT. While this potential geometry suggests that the $(GT)_6$ rings may have coordinated directionality, wrapping in opposite directions from each other along the SWCNT, this proposed mechanism would require further investigation without the presence of the AuNP tag to prove definitively. These findings attest to the complexity of these nanobiotechnologies, suggesting that the mechanisms behind their molecular recognition could be conformationally driven, underscoring the need for rational design to properly tailor their optical properties. Future XSI experiments could serve to investigate both the sequence specificity observed in analyte recognition (for example, catecholamine recognition by $(GT)_n$ that is absent for $(GA)_n$[43] and in SWCNT chirality sorting

(for example, $(TAT)_4$ with its recognition partner, the (6,5) SWCNT).[57]

Although no AuNP size dependence was observed over a range of 5.9−7.2 nm diameter and the TEM analysis suggests that we have not reached the close-packing limit, it is yet unclear how the AuNP tags affect the ssDNA on the SWCNT surface. Additionally, surface coverage calculations as well as MD simulations[43] indicate that ssDNA may pack in closer spacing than this technique can currently observe since the intra-AuNP peak may be obscuring shorter distances. In future experiments, smaller AuNPs (on the order of 1 nm diameter) could be used to confirm and expand upon these findings. At these smaller AuNP sizes, both the spatial resolution and the lower observable range of distances would be improved; however, the electron density would be on the same order as that of the ssDNA and SWCNTs and thus become more mathematically difficult to deconvolute.

In summary, we demonstrate that XSI can be applied to characterize DNA-based nanotechnologies under biologically relevant, solution-phase conditions, complementing existing techniques. Notably, XSI in parallel to spectroscopic measurements will allow exploration of geometric and mechanistic rationale for changes in fluorescence response to target analytes and should assist in developing rational design strategies for these materials. Through this approach, we gain an understanding of the discrete nanoscale architectures of these materials and their mechanisms of interaction with the local ionic environment in solution and with target analytes for sensing. XSI will enable the higher-throughput study of polymer−nanoparticle complexes for a broad range of nanobiotechnology applications.

■ METHODS

Synthesis of Citrate-Capped Gold Nanoparticles (AuNPs). Citrate-capped AuNPs of diameters 5.9−7.2 nm were prepared using a method modified from that which was previously described.[58] Briefly, a 2 L solution of 0.25 mM $HAuCl_4$ and 0.25 mM trisodium citrate was prepared in a conical flask using ddH_2O cooled to 4 °C. Next, 10 mL of 0.6 M $NaBH_4$ at 4 °C was added rapidly to the solution while stirring. The solution turned dark red immediately after addition of $NaBH_4$, indicating particle formation. The solution was allowed to warm to room temperature (RT) and stirred overnight with no reactivity from excess $NaBH_4$.

Citrate-BSPP Exchange for Gold Nanoparticles (BSPP-AuNPs). Bis(p-sulfonatophenyl) phenylphosphine (BSPP) was added to citrate-stabilized colloidal AuNPs (approximately 5.0×10^{13} particles/mL) to a final concentration of 0.5 g/L and stirred at RT for a minimum of 6 h. Approximately 1 mL of saturated NaCl solution was added per 10 mL of BSPP-exchanged colloidal gold, until the solution changed from transparent red to a darker, cloudy purple, indicating the reversible precipitation of the AuNPs.[59] The mixture was centrifuged (Beckman Coulter, Avanti J25, JA-18 rotor, Indianapolis, IN) at 12,000 rcf for 10 min, and the supernatant was decanted to waste. BSPP-AuNPs were washed twice with 0.5 M NaCl solution (repeating the centrifugation step above) and resuspended in 15 mM phosphate buffer and 1 mM tris(2-carboxyethyl) phosphine hydrochloride (TCEP), pH 7 for storage. Suspensions were stored at 4 °C until use. Note that freezing caused sample precipitation. Unless specified otherwise, all reagents were purchased from Millipore Sigma (Burlington, MA).

Conjugation of Single-Stranded DNA to BSPP-AuNPs (ssDNA-AuNPs). If stored longer than 2 weeks, fresh TCEP was added to reduce the solution of colloidal BSPP-AuNPs prior to ssDNA conjugation by adding saturated NaCl solution to BSPP-AuNPs until the solution turned dark/cloudy, centrifuging at 12,000 rcf for 10 min, and resuspending in fresh 15 mM phosphate buffer, 1

mM TCEP, pH 7. The final BSPP-AuNP concentration was determined by measuring the absorbance at 520 nm (NanoDrop 2000, Thermo Scientific) and converting to concentration with the empirical extinction coefficient,[60] $\varepsilon_{520nm} = 9.69 \times 10^6$ L mol^{-1} cm^{-1}. The concentration of the desired oligonucleotides was calculated by measuring the absorbance at 260 nm using the sequence-dependent extinction coefficient. BSPP-AuNPs were attached to ssDNA via trithiolated linkers (Letsinger's type) on the 5′-end of ssDNA oligomers with SDS-PAGE purification (Fidelity Systems, Gaithersburg, MD) by mixing at a 1:1 molar ratio and incubating at RT overnight. Conjugated ssDNA-AuNPs were then coated with short, neutral methoxy poly(ethylene glycol) thiol (mPEG-SH; MW approximately 350 g/mol; Biochempeg Scientific Inc., Watertown, MA), by adding mPEG-SH to the ssDNA-AuNP suspension at a final molar ratio of 3000:1 mPEG-SH to AuNPs.

Anion-Exchange Chromatography Purification of ssDNA-AuNPs. Monoconjugated ssDNA-AuNPs were isolated as previously described[39,40] using a Dionex DNA-Pac PA100 anion-exchange column on either a GE AKTA Explorer or a GE Atka Pure fast protein liquid chromatography (FPLC; General Electric HealthCare Technologies, Chicago, IL) with an NaCl gradient from 0.01 to 1 M over a period of 55 min at a flow rate of 1.1 mL/min. Sample elution was monitored by measuring ultraviolet−visible (UV−vis) absorption at 260 (ssDNA) and 520 nm (AuNPs), and the monoconjugated ssDNA-AuNP fraction was collected for downstream use (Figure S2A). Importantly, the first peak of the anion-exchange chromatogram is neutrally charged PEG-AuNP, as negatively charged materials remain adsorbed to the column. Monoconjugated ssDNA-AuNPs structures were confirmed by agarose gel electrophoresis as previously described.[61] The same AuNP conjugation and purification method was implemented for both $(GT)_{15}$ and $(GT)_6$ oligomers, with the longer oligomers demonstrating increased retention times via anion-exchange chromatography, as expected (Figure S2B). The final ssDNA-AuNP concentration was determined again by measuring absorbance.

Data Collection and Processing by High-Throughput X-ray Scattering Interferometry (HT-XSI). HT-XSI data was collected at the SIBYLS beamline (bl12.3.1) at the Advanced Light Source of Lawrence Berkeley National Laboratory, Berkeley, California.[62] The X-ray wavelength was set at λ = 0.12398 nm, and the sample-to-detector distance was 2.07 m, resulting in a scattering vector (q) range of 0.1−4.6 nm^{-1}, which corresponds to real-space distances of 62.8−1.4 nm. The scattering vector is defined as $q = 4\pi \sin\theta/\lambda$, with a scattering angle 2θ. Data was collected using a Dectris PILATUS3X 2 M detector and processed as described previously.[42]

Immediately prior to data collection, 15 μL of each sample was added to 15 μL of buffer in a 96-well plate for final corresponding concentrations of 42.5−450 nM ssDNA-AuNPs and 0.17−1.76 mg/L SWCNTs. Each sample was then transferred to the XSI sampling position via a Tecan Evo liquid handling robot (Tecan Trading AG, Switzerland) with modified pipetting needles acting as sample cells as described previously.[41] Samples were exposed to X-ray synchrotron radiation for 5 s at a 0.1 s frame rate for a total of 50 images. Each collected image was circularly integrated and normalized for beam intensity to generate a 1D scattering profile. Buffer subtraction was performed for the one-dimensional scattering profile of each sample using each of two surrounding buffer wells to ensure that the subtraction process was not subject to instrument variations. Scattering profiles over 5 s exposure were sequentially averaged together to eliminate any potential radiation damage effects. All data processing was done using our beamline specific data-processing pipeline by the SIBYLS SAXS Process (SSP) GUI.[40,63] Pairwise distribution functions, $P(r)$, were generated in batch using the automated GNOM[64] feature of the SSP GUI. All scattering data used in this manuscript was deposited into the Simple Scattering database used for depositing correlated scattering data sets under accession number XSEVJCYK and are available at the following URL: https://simplescattering.com/dataset/XSEVJCYK.

Characterization by Small-Angle X-ray Scattering (SAXS). Average SWCNT bundling of ssDNA-SWCNTs (no AuNPs)

determined by calculating the cross-sectional radius of gyration for rod-like scatterers from SAXS curves using ATSAS 3.0.[65] Absolute-scale intensity scattering measurements and calculations were completed as previously described.[66] All AuNPs used in this study are near-spherical, with average diameters ranging from 5.9 to 7.2 nm determined from pairwise distribution functions, $P(r)$, obtained from SAXS curves for each batch of synthesized ssDNA-AuNPs (Figure S3A and Tables S1 and S2). SAXS profiles for all ssDNA-AuNPs were further modeled as triaxial ellipsoidal fittings[67] using SasView software to obtain more accurate nanoparticle dimensions (Figure S3B and Tables S1 and S2 and detailed in Supporting Information, Section S.6). The average ratio of the largest (major equatorial radius, r_A) to smallest (polar radius, r_C) particle dimension is observed at 3.3:2. Including a polydispersity parameter for r_A was essential to optimize the fit (Figure S3C). The average polydispersity index (PDI) of r_A is 0.18, indicating reasonable monodispersity, where PDI < 0.1 is considered ideal.[68]

Electron Density Calculations. For X-ray scattering experiments, the electron density of a material is of critical importance as the total scattering intensity is proportional to the square of the electron density. The triaxial ellipsoidal AuNPs used in this study have a calculated electron density of 3519.08 e$^-$/nm^3, increasing the electron density of our otherwise low-scattering materials with calculated electron densities of 914.3 and 1818 e$^-$/nm^3 for SWCNTs and ssDNA, respectively. Detailed electron density calculations are found in Supporting Information, Section S.1.

Characterization by Dynamic Light Scattering (DLS). DLS measurements were taken with the Zetasizer Nano ZS (Malvern Analytical) with a material refractive index of 0.200 and absorption of 3.320 for colloidal gold.[69,70] All samples were diluted in 0.1× phosphate-buffered saline (PBS; note 1× PBS is 137 mM NaCl, 2.7 mM KCl, 10 mM Na$_2$HPO$_4$, and 1.8 mM KH$_2$PO$_4$, pH 7.4) to an AuNP concentration of 0.20−0.25 μM and loaded in disposable cuvettes (Malvern ZEN0040) for size measurement. AuNPs were coated with mPEG-SH to prevent aggregation and aid in the purification by anion-exchange chromatography.[39] After mPEG-SH coating, the hydrodynamic radii of the AuNPs measured by DLS increase from the AuNP core radii measured with SAXS by an average of 1.46 ± 0.34 nm across all samples (Figure S3D and Table S3). This increase in hydrodynamic diameter implies successful mPEG-SH functionalization of the exposed AuNP surfaces.[71] The average length of the mPEG-SH (of MW 350 g/mol) is approximately 1.7 nm when fully extended, based on the length of the repeating poly(ethylene oxide) unit of 0.278 nm in water (with $n = 6$ units total).[72] However, even if all available mPEG-SH functionalized the surface, the theoretical distance between grafting sites (approximately 5.2 nm) would far exceed the calculated Flory radius of 0.815 nm, leading to only a partially extended mushroom conformation. This result is in line with the measured change in hydrodynamic radius imparted by mPEG-SH being slightly less than the expected change based on polymer length.[73−75]

Suspension of Single-Walled Carbon Nanotubes (SWCNTs) with ssDNA-AuNPs. ssDNA-AuNP concentration was determined by measuring the absorbance at 520 nm (NanoDrop One, Thermo Scientific) with a 10×-diluted aliquot and calculating the concentration as before. Single-walled carbon nanotubes (SWCNTs) were suspended with ssDNA-AuNPs as follows: mixed-chirality raw SWCNTs (small diameter HiPco SWCNTs, raw, NanoIntegris, Boisbriand, Quebec, Canada) were first prepared as an aqueous slurry of 2 mg/mL in Milli-Q water. ssDNA-AuNP-SWCNTs were then formulated to maintain a final ratio of 250 nmol ssDNA-AuNP per 1 mg SWCNT, at a total volume of 2−4 mL (such that half of the solution could serve as nonsonication controls). The exact formulation recipe depended on the yield of ssDNA-AuNPs obtained after anion-exchange purification. For every 2 mL of ssDNA-AuNPs at 200−800 nM (0.4−1.6 nmol), 0.8−3.2 μL of SWCNT slurry was added (1.6−6.4 μg) in 0.1× phosphate-buffered saline (PBS; note 1× PBS is 137 mM NaCl, 2.7 mM KCl, 10 mM Na$_2$HPO$_4$, 1.8 mM KH$_2$PO$_4$, pH 7.4) in a 5 mL tube. The ssDNA-AuNP/SWCNT mixture was bath-sonicated for 10 min (Branson Ultrasonic 1800)

and then probe-tip-sonicated for 10 min in an ice bath (3 mm probe tip at 50% amplitude, 5−6 W, Cole-Parmer Ultrasonic Processor). ssDNA-AuNP-SWCNT suspension was equilibrated for 30 min at RT then dialyzed against 2 L of 0.1× PBS overnight (200 μL volume in Pur-A-Lyzer Mini Dialysis Kit with 6−8 kDa MWCO, Millipore Sigma). Note that free ssDNA-AuNPs are not expected to pass through this filter size that contains pores of only a few nanometers, and this step was included as a buffer exchange to remove any impurities still present from the AuNP synthesis. Suspensions were stored at 4 °C until use. Control experiments without SWCNTs were prepared from the same batch of ssDNA-AuNPs, with all steps being the same but in the absence of SWCNTs.

Certain parameters were slightly modified in comparison to usual ssDNA-SWCNT suspension protocols to account for the AuNP tag on the ssDNA. First, the material amounts were reduced approximately 2 orders of magnitude to account for the limited availability of AuNPs, although kept in a similar ratio to previous suspension protocols (250 nmol of ssDNA:1 mg of SWCNT).[11,45] Second, a postsonication pelleting step, which one would typically perform in order to remove unsuspended SWCNTs or amorphous carbon and catalyst left over from SWCNT synthesis, was omitted because the presence of the AuNPs causes full sample pelleting due to the additional mass. We expect that reducing the overall material load by 2 orders of magnitude also reduced the concentration of SWCNT-derived impurities in the final suspension, thus eliminating the need for a centrifugation cleanup step. Finally, SWCNT suspensions were not spin-filtered due to embedding of the AuNPs into the filter membrane and full sample loss. Unless specified, all reagents, including Carboxylated SWCNTs used for controls, were purchased from Millipore Sigma (Burlington, MA). Additional suspension notes and controls are detailed in Supporting Information, Section S.2.

Characterization by Absorbance and Fluorescence. Absorbance was measured with a UV−vis−near-infrared (UV−vis−NIR) spectrophotometer (UV-3600 Plus, Shimadzu Corporation, Kyoto, Kyoto, Japan) using a 50 μL sample volume in a black-sided quartz cuvette (Thorlabs, Inc., Newton, NJ). Near-infrared SWCNT fluorescence was measured using an inverted Zeiss microscope (Axio Observer.D1, 10× objective, Carl-Zeiss-Stiftung, Oberkochen, Baden-Württemberg, Germany) with a Princeton Instruments spectrometer (SCT 320) and a liquid nitrogen-cooled Princeton Instruments InGaAs detector (PyLoN-IR; Teledyne Technologies, Thousand Oaks, CA). A triggered 721 nm laser (OptoEngine LLC, Midvale, UT) was used as the excitation source, and fluorescence emission was collected from 800 to 1400 nm. 30 μL volume of each sample was prepared in polypropylene 384 well plates (Greiner Bio-One microplate). Near-infrared fluorescence responses of ssDNA-AuNP-SWCNTs were characterized using the same microscope setup and using 100 μL of the ssDNA-AuNP-SWCNT nanosensor per 384 well plate, with fluorescence spectra recorded before and after the addition of 1 μL of 10 mM analyte (DA or TY).

Characterization by Transmission Electron Microscopy (TEM). Images of (GT)$_{15}$- and (GT)$_6$-AuNP-SWCNT complexes were captured using a Tecnai 12 TEM (FEI, Hillsboro, OR) operating at an accelerating voltage of 120 kV, and data was recorded using a Gatan Rio16 CMOS camera with GWS software (Gatan Inc., Pleasanton, CA). Samples were prepared by depositing 5 μL of sample onto 400 mesh carbon/Formvar-coated copper grids (Electron Microscopy Science (EMS)) that were surface-treated by glow discharge to render the support hydrophilic. The samples were wicked away after 2 min. No negative staining or washing steps were included. Approximately 20 images were taken at four different regions on the grid for each sample to ensure that reported images were representative. Additional image analysis was performed using Fiji (Imagej2).[76] To determine the size distribution and average AuNP size, over 4000 AuNPs were analyzed. To estimate the AuNP packing on the SWCNTs, a minimum of five SWCNTs were analyzed per sample, resulting in a total SWCNT length of ≥3140 nm. To measure the inter-AuNP axial distances along the SWCNTs, over 620 inter-AuNP distances were analyzed per sample by manually

measuring the center-to-center inter-AuNP distances of nearest neighbors axially on separate sides of the SWCNT.

***Ab Initio* Modeling of XSI Data.** Modeling of the scattering profiles were done using SASHEL, adapting the methodology originally described by Burian and Amenitsch.[77] SASHEL was first developed as an algorithm to reconstruct helical and rod-like systems by randomly moving dummy atoms comprising a single building block unit and projecting them outward using symmetrical boundary conditions. Theoretical scattering profiles from these projected models are iteratively fit to experimental data to converge on the best-fit model. In a typical SASHEL analysis, it is recommended to reduce the number of total data points uniformly across the original 1D curve (*i.e.*, removing every other data point) to lower calculation times. However, this leads to a higher density of data points in the high q-range due to the binning of the circular integration of the detector images and reduces the fitting quality in the low q-range. In this study, data points were sequentially removed at higher density as the q-value increases to retain high fit quality in the low q-range, corresponding to the longer order distances of interest. The data was fit over a truncated q-range of 0.1−3 nm^{-1} to further focus on the lower q-range.

Initial conditions for the model were refined over many iterations, with the most robust outcome derived from a carefully curated starting model for both the $(GT)_{15}$- and $(GT)_6$-AuNP-SWCNT samples (Figure S19). First, the more clearly defined $(GT)_6$-AuNP-SWCNT scattering curve was used to produce a crude initial estimate of dummy-atom positions (Figure S19A). This model started with a core−shell cylinder model with a 15 nm outer diameter and 5 nm inner diameter, as determined by the average diameter of the SWCNT (1 nm) together with a fully extended trithiolated linker on either side (2 nm each). The stack building block height (H_{BB}) was set equal to the axial inter-AuNP distance (17.2 nm) of $(GT)_6$-AuNP-SWCNT, as determined from $P(r)$ functions (Figure 1B). The number of stacks (N_S) was set to 15 to ensure an overall length far greater than the observed maximum length dimension, d_{max}, of the $(GT)_6$-AuNP-SWCNT samples (55 nm). The starting temperature (T_0) was set to 0.6 to allow for broad movement of 2000 initial dummy atoms per H_{BB}. T_0 in this case is the value in which the system starts to cool down as defined previously[77] and is not representative of temperature on an absolute scale. Dummy-atom diameters were set to 0.288 nm to simulate the atomic diameter of a gold atom. From this initial model, clusters of dummy atoms formed and were taken to be naturally representative of AuNPs (regions with high electron density). The most clearly defined cluster was extracted, duplicated to create a pair of AuNPs, and the number of dummy atoms expanded to 1000 for each AuNP (Figure S19A).

Each AuNP in the initial pair is maneuvered into estimated initial geometries as determined experimentally to represent the inter-AuNP block heights (H_{GB}) unique for $(GT)_{15}$- and $(GT)_6$-AuNP-SWCNTs (14.3 and 17.2 nm, respectively). Each refined AuNP pair (H_{GB} unit) was then replicated axially using symmetrical boundary conditions an integer (k) number of times to produce a total stack height, $H_{BB} = k \times H_{GB}$, as depicted in Figure S19B,C for $(GT)_{15}$- and $(GT)_6$-AuNP-SWCNTs, respectively. After exploring a large parameter space (outlined in detail in Supporting Information, Section S.4, Tables S4, S5 and Figures S20−S23), it was discovered that when so few dummy atoms were used per AuNP, the models would fit better by expanding outward to compensate for a lack of representative electron density. Thus, initially modeling $(GT)_{15}$- and $(GT)_6$-AuNP-SWCNTs as two neighboring ssDNA-AuNP-SWCNTs saved a lot of computational time (fewer dummy atoms to move per iteration) and allowed for a larger parameter space to be explored. These initial models were run at a starting temperature of 0.2 at each of the respective H_{BB} values, with $N_S = 32$/number of AuNPs (N_{NP}) rounded to the nearest integer value, where N_{NP} is the total number of AuNPs per stack. All models were run for 200 iterations as the goodness of fit (χ^2-value) tends to reach a minimum plateau.

To model the system as a single SWCNT, the best-fit double SWCNT model for $(GT)_{15}$- and $(GT)_6$-AuNP-SWCNT was selected (Figure S24) and the single SWCNT region showing the clearest AuNP spacing is extracted. The regions of clear electron density are replaced with denser 3000 dummy-atom clusters (representing AuNPs; Figure S19B,C), and an initial H_{BB} was used which resulted in the best fit from each respective double SWCNT model (H_{BB} = 114.5 and 155.2 nm for $(GT)_{15}$- and $(GT)_6$-AuNP-SWCNT respectively; Table S5 and Figure S23). The N_S values were 3 and 2 for $(GT)_{15}$- and $(GT)_6$-AuNP-SWCNT models, respectively, to obtain final models of similar total lengths (342.6 and 310.4 nm, respectively). Over many iterations, as regions in the model appeared that suggested areas of excessive or missing electron density, AuNPs (dummy-atom clusters) were manually removed or added accordingly until achieving a best fitting single SWCNT model (Figure S14A,B). Higher starting temperatures ($T_0 > 0.4$) were generally used for single SWCNT to speed up the movement of initial models containing at least 3-fold more dummy atoms than earlier models.

■ ASSOCIATED CONTENT

Ⓢ Supporting Information

The Supporting Information is available free of charge at https://pubs.acs.org/doi/10.1021/jacs.3c09549.

> Extended discussion and methods Sections S.1−S.6 (Electron density calculations, ssDNA-AuNP-SWCNT alternative methods, TEM analysis, *ab initio* modeling, geometric and surface coverage calculations, and triaxial ellipsoidal fitting calculations); Figures S1−S25 (scattering profiles of ssDNA-AuNP-SWCNTs and controls, characterization of synthesized ssDNA-AuNPs and ssDNA-AuNP-SWCNTs, pairwise distribution functions and scattering curves, TEM images and analysis, *ab initio* modeling optimization and results, ssDNA-AuNP-SWCNT response to dopamine and schematic of possible dopamine interaction); Tables S1−S5 (characterization of synthesized ssDNA-AuNPs and SASHEL modeling parameters and results). (PDF)

■ AUTHOR INFORMATION

Corresponding Author

Rebecca L. Pinals − *Picower Institute for Learning and Memory, Massachusetts Institute of Technology, Cambridge, Massachusetts 02139, United States; Department of Brain and Cognitive Sciences, Massachusetts Institute of Technology, Cambridge, Massachusetts 02139, United States;* ⬤ orcid.org/0000-0002-5369-2317; Email: rpinals@mit.edu

Authors

Daniel J. Rosenberg − *Graduate Group in Biophysics, University of California, Berkeley, Berkeley, California 94720, United States; Molecular Biophysics and Integrated Bioimaging, Lawrence Berkeley National Laboratory, Berkeley, California 94720, United States; Linac Coherent Light Source, SLAC National Accelerator Laboratory, Menlo Park, California 94025, United States;* ⬤ orcid.org/0000-0001-8017-8156

Francis J. Cunningham − *Department of Chemical and Biomolecular Engineering, University of California, Berkeley, Berkeley, California 94720, United States*

Joshua D. Hubbard − *Department of Chemical and Biomolecular Engineering, University of California, Berkeley, Berkeley, California 94720, United States*

Natalie S. Goh − *Department of Chemical and Biomolecular Engineering, University of California, Berkeley, Berkeley, California 94720, United States*

Jeffrey Wei-Ting Wang − *Department of Chemical and Biomolecular Engineering, University of California, Berkeley, Berkeley, California 94720, United States*

Shoichi Nishitani − *Department of Chemical and Biomolecular Engineering, University of California, Berkeley, Berkeley, California 94720, United States;* ⊙ orcid.org/0000-0001-6355-6952

Emily B. Hayman − *Molecular Biophysics and Integrated Bioimaging, Lawrence Berkeley National Laboratory, Berkeley, California 94720, United States; Department of Chemical and Biomolecular Engineering, University of California, Berkeley, Berkeley, California 94720, United States*

Greg L. Hura − *Molecular Biophysics and Integrated Bioimaging, Lawrence Berkeley National Laboratory, Berkeley, California 94720, United States; Chemistry and Biochemistry Department, University of California Santa Cruz, Santa Cruz, California 95064, United States;* ⊙ orcid.org/0000-0003-0501-8464

Markita P. Landry − *Department of Chemical and Biomolecular Engineering and California Institute for Quantitative Biosciences, QB3, University of California, Berkeley, Berkeley, California 94720, United States; Chan-Zuckerberg Biohub, San Francisco, California 94158, United States; Innovative Genomics Institute (IGI), Berkeley, California 94720, United States;* ⊙ orcid.org/0000-0002-5832-8522

Complete contact information is available at:
https://pubs.acs.org/10.1021/jacs.3c09549

Notes

The authors declare no competing financial interest.

■ ACKNOWLEDGMENTS

■ REFERENCES

(1) Ackermann, J.; Metternich, J. T.; Herbertz, S.; Kruss, S. Biosensing with Fluorescent Carbon Nanotubes. *Angew. Chem., Int. Ed.* **2022**, *61*, No. e202112372, DOI: 10.1002/anie.202112372.

(2) Antonucci, A.; Kupis-Rozmysłowicz, J.; Boghossian, A. A. Noncovalent Protein and Peptide Functionalization of Single-Walled Carbon Nanotubes for Biodelivery and Optical Sensing Applications. *ACS Appl. Mater. Interfaces* **2017**, *9*, 11321−11331.

(3) Kruss, S.; Landry, M. P.; Ende, E. V.; et al. Neurotransmitter Detection Using Corona Phase Molecular Recognition on Fluorescent Single-Walled Carbon Nanotube Sensors. *J. Am. Chem. Soc.* **2014**, *136*, 713−724, DOI: 10.1021/ja410433b.

(4) Bisker, G.; Dong, J.; Park, H. D.; et al. Protein-targeted corona phase molecular recognition. *Nat. Commun.* **2016**, *7*, No. 10241.

(5) Pinals, R. L.; Ledesma, F.; Yang, D.; et al. Rapid SARS-CoV-2 Spike Protein Detection by Carbon Nanotube-Based Near-Infrared Nanosensors. *Nano Lett.* **2021**, *21*, 2272−2280.

(6) Hong, G.; Diao, S.; Chang, J.; et al. Through-skull fluorescence imaging of the brain in a new near-infrared window. *Nat. Photonics* **2014**, *8*, 723−730.

(7) Godin, A. G.; Varela, J. A.; Gao, Z.; et al. Single-nanotube tracking reveals the nanoscale organization of the extracellular space in the live brain. *Nat. Nanotechnol.* **2017**, *12*, 238−243.

(8) Demirer, G. S.; Zhang, H.; Matos, J. L.; et al. High aspect ratio nanomaterials enable delivery of functional genetic material without DNA integration in mature plants. *Nat. Nanotechnol.* **2019**, *14*, 456−464, DOI: 10.1038/s41565-019-0382-5.

(9) Boyer, P. D.; Ganesh, S.; Qin, Z.; et al. Delivering Single-Walled Carbon Nanotubes to the Nucleus Using Engineered Nuclear Protein Domains. *ACS Appl. Mater. Interfaces* **2016**, *8*, 3524−3534.

(10) Bates, K.; Kostarelos, K. Carbon nanotubes as vectors for gene therapy: Past achievements, present challenges and future goals. *Adv. Drug Delivery Rev.* **2013**, *65*, 2023−2033.

(11) Beyene, A. G.; Delevich, K.; Del Bonis-O'Donnell, J. T.; et al. Imaging striatal dopamine release using a nongenetically encoded near infrared fluorescent catecholamine nanosensor. *Sci. Adv.* **2019**, *5*, No. eaaw3108, DOI: 10.1126/sciadv.aaw3108.

(12) Kruss, S.; Salem, D. P.; Vuković, L.; et al. High-resolution imaging of cellular dopamine efflux using a fluorescent nanosensor array. *Proc. Natl. Acad. Sci. U.S.A.* **2017**, *114*, 1789−1794.

(13) Bulumulla, C.; Krasley, A. T.; Cristofori-Armstrong, B.; et al. Visualizing synaptic dopamine efflux with a 2D composite nanofilm. *eLife* **2022**, *11*, No. e78773, DOI: 10.7554/eLife.78773.

(14) Elizarova, S.; Chouaib, A. A.; Shaib, A.; et al. A fluorescent nanosensor paint detects dopamine release at axonal varicosities with high spatiotemporal resolution. *Proc. Natl. Acad. Sci. U.S.A.* **2022**, *119*, No. e2202842119, DOI: 10.1073/pnas.2202842119.

(15) Jeong, S.; Yang, D.; Beyene, A. G.; et al. High-throughput evolution of near-infrared serotonin nanosensors. *Sci. Adv.* **2019**, *5*, No. eaay3771, DOI: 10.1126/sciadv.aay3771.

(16) Dinarvand, M.; Neubert, E.; Meyer, D.; et al. Near-Infrared Imaging of Serotonin Release from Cells with Fluorescent Nanosensors. *Nano Lett.* **2019**, *19*, 6604−6611.

(17) Wu, H.; Nißler, R.; Morris, V.; et al. Monitoring Plant Health with Near-Infrared Fluorescent H_2O_2 Nanosensors. *Nano Lett.* **2020**, *20*, 2432−2442.

(18) Safaee, M. M.; Gravely, M.; Roxbury, D. A Wearable Optical Microfibrous Biomaterial with Encapsulated Nanosensors Enables Wireless Monitoring of Oxidative Stress. *Adv. Funct. Mater.* **2021**, *31*, No. 2006254, DOI: 10.1002/adfm.202006254.

(19) Lew, T. T. S.; Koman, V. B.; Silmore, K. S.; et al. Real-time detection of wound-induced H_2O_2 signalling waves in plants with optical nanosensors. *Nat. Plants* **2020**, *6*, 404−415.

(20) Iverson, N. M.; Barone, P. W.; Shandell, M.; et al. In vivo biosensing via tissue-localizable near-infrared-fluorescent single-walled carbon nanotubes. *Nat. Nanotechnol.* **2013**, *8*, 873−880.

(21) Zhang, J.; Boghossian, A. A.; Barone, P. W.; et al. Single Molecule Detection of Nitric Oxide Enabled by d(AT)15 DNA Adsorbed to Near Infrared Fluorescent Single-Walled Carbon Nanotubes. *J. Am. Chem. Soc.* **2011**, *133*, 567−581.

(22) Alizadehmojarad, A. A.; Zhou, X.; Beyene, A. G.; et al. Binding Affinity and Conformational Preferences Influence Kinetic Stability of Short Oligonucleotides on Carbon Nanotubes. *Adv. Mater. Interfaces* **2020**, *7*, No. 2000353, DOI: 10.1002/admi.202000353.

(23) Landry, M. P.; Vuković, L.; Kruss, S.; et al. Comparative Dynamics and Sequence Dependence of DNA and RNA Binding to Single Walled Carbon Nanotubes. *J. Phys. Chem. C* **2015**, *119*, 10048−10058.

(24) Campbell, J. F.; Tessmer, I.; Thorp, H. H.; Erie, D. A. Atomic Force Microscopy Studies of DNA-Wrapped Carbon Nanotube Structure and Binding to Quantum Dots. *J. Am. Chem. Soc.* **2008**, *130*, 10648−10655.

(25) Zheng, M.; Jagota, A.; Semke, E. D.; et al. DNA-assisted dispersion and separation of carbon nanotubes. *Nat. Mater.* **2003**, *2*, 338−342.

(26) Kwak, S.-Y.; Lew, T. T. S.; Sweeney, C. J.; et al. Chloroplast-selective gene delivery and expression in planta using chitosan-complexed single-walled carbon nanotube carriers. *Nat. Nanotechnol.* **2019**, *14*, 447−455.

(27) Zheng, M.; Jagota, A.; Strano, M. S.; et al. Structure-Based Carbon Nanotube Sorting by Sequence-Dependent DNA Assembly. *Science* **2003**, *302*, 1545−1548.

(28) Safaee, M. M.; Gravely, M.; Rocchio, C.; Simmeth, M.; Roxbury, D. DNA Sequence Mediates Apparent Length Distribution in Single-Walled Carbon Nanotubes. *ACS Appl. Mater. Interfaces* **2019**, *11*, 2225−2233.

(29) Hough, L. A.; Islam, M. F.; Hammouda, B.; Yodh, A. G.; Heiney, P. A. Structure of Semidilute Single-Wall Carbon Nanotube Suspensions and Gels. *Nano Lett.* **2006**, *6*, 313−317.

(30) Barrejón, M.; Syrgiannis, Z.; Burian, M.; et al. Cross-Linked Carbon Nanotube Adsorbents for Water Treatment: Tuning the Sorption Capacity through Chemical Functionalization. *ACS Appl. Mater. Interfaces* **2019**, *11*, 12920−12930, DOI: 10.1021/acsami.8b20557.

(31) Pinals, R. L.; Yang, D.; Rosenberg, D. J.; et al. Quantitative Protein Corona Composition and Dynamics on Carbon Nanotubes in Biological Environments. *Angew. Chem., Int. Ed.* **2020**, *59*, 23668−23677.

(32) Demirer, G. S.; Zhang, H.; Goh, N. S.; et al. Carbon nanocarriers deliver siRNA to intact plant cells for efficient gene knockdown. *Sci. Adv.* **2020**, *6*, No. eaaz0495, DOI: 10.1126/sciadv.aaz0495.

(33) Putnam, C. D.; Hammel, M.; Hura, G. L.; Tainer, J. A. X-ray solution scattering (SAXS) combined with crystallography and computation: defining accurate macromolecular structures, conformations and assemblies in solution. *Q. Rev. Biophys.* **2007**, *40*, 191−285, DOI: 10.1017/S0033583507004635.

(34) Mathew-Fenn, R. S.; Das, R.; Harbury, P. A. B. Remeasuring the Double Helix. *Science* **2008**, *322*, 446−449.

(35) Mathew-Fenn, R. S.; Das, R.; Silverman, J. A.; Walker, P. A.; Harbury, P. A. B. A Molecular Ruler for Measuring Quantitative Distance Distributions. *PLoS One* **2008**, *3*, No. e3229, DOI: 10.1371/journal.pone.0003229.

(36) Shi, X.; Beauchamp, K. A.; Harbury, P. B.; Herschlag, D. From a structural average to the conformational ensemble of a DNA bulge. *Proc. Natl. Acad. Sci. U.S.A.* **2014**, *111*, E1473−E1480.

(37) Shi, X.; Herschlag, D.; Harbury, P. A. B. Structural ensemble and microscopic elasticity of freely diffusing DNA by direct measurement of fluctuations. *Proc. Natl. Acad. Sci. U.S.A.* **2013**, *110*, E1444−E1451.

(38) Zettl, T.; Das, R.; Harbury, P. A. B.; et al. Recording and Analyzing Nucleic Acid Distance Distributions with X-Ray Scattering Interferometry (XSI). *Curr. Protoc. Nucleic Acid Chem.* **2018**, *73*, No. e54, DOI: 10.1002/cpnc.54.

(39) Hura, G. L.; Tsai, C. L.; Claridge, S. A.; et al. DNA conformations in mismatch repair probed in solution by X-ray scattering from gold nanocrystals. *Proc. Natl. Acad. Sci. U.S.A.* **2013**, *110*, 17308−17313.

(40) Rosenberg, D. J.; Syed, A.; Tainer, J. A.; Hura, G. L. Monitoring Nuclease Activity by X-Ray Scattering Interferometry Using Gold Nanoparticle-Conjugated DNA. In *DNA Damage Responses*; Mosammaparast, N., Ed.; Methods in Molecular Biology; Springer US, 2022; Vol. *2444*, pp 183−205.

(41) Hura, G. L.; Menon, A. L.; Hammel, M.; et al. Robust, high-throughput solution structural analyses by small angle X-ray scattering (SAXS). *Nat. Methods* **2009**, *6*, 606−612.

(42) Dyer, K. N.; Hammel, M.; Rambo, R. P.et al. High-Throughput SAXS for the Characterization of Biomolecules in Solution: A Practical Approach. In *Structural Genomics: General Applications*; Chen, Y. W., Ed.; Methods in Molecular Biology; Humana Press, 2014; pp 245−258.

(43) Beyene, A. G.; Alizadehmojarad, A. A.; Dorlhiac, G.; et al. Ultralarge Modulation of Fluorescence by Neuromodulators in Carbon Nanotubes Functionalized with Self-Assembled Oligonucleotide Rings. *Nano Lett.* **2018**, *18*, 6995−7003.

(44) Pinals, R. L.; Yang, D.; Lui, A.; Cao, W.; Landry, M. P. Corona Exchange Dynamics on Carbon Nanotubes by Multiplexed Fluorescence Monitoring. *J. Am. Chem. Soc.* **2020**, *142*, 1254−1264.

(45) Yang, D.; Yang, S. J.; Del Bonis-O'Donnell, J. T.; Pinals, R. L.; Landry, M. P. Mitigation of Carbon Nanotube Neurosensor Induced Transcriptomic and Morphological Changes in Mouse Microglia with Surface Passivation. *ACS Nano* **2020**, *14*, 13794−13805.

(46) Weisman, R. B.; Bachilo, S. M. Dependence of Optical Transition Energies on Structure for Single-Walled Carbon Nanotubes in Aqueous Suspension: An Empirical Kataura Plot. *Nano Lett.* **2003**, *3*, 1235−1238.

(47) Putnam, C. D.; Hammel, M.; Hura, G. L.; Tainer, J. A. X-ray solution scattering (SAXS) combined with crystallography and computation: defining accurate macromolecular structures, conformations and assemblies in solution. *Q. Rev. Biophys.* **2007**, *40*, 191−285, DOI: 10.1017/S0033583507004635.

(48) Bergmann, A.; Fritz, G.; Glatter, O. Solving the generalized indirect Fourier transformation (GIFT) by Boltzmann simplex simulated annealing (BSSA). *J. Appl. Crystallogr.* **2000**, *33*, 1212−1216.

(49) Johnson, R. R.; Johnson, A. T. C.; Klein, M. L. Probing the Structure of DNA−Carbon Nanotube Hybrids with Molecular Dynamics. *Nano Lett.* **2008**, *8*, 69−75.

(50) Cathcart, H.; Nicolosi, V.; Hughes, J. M.; et al. Ordered DNA Wrapping Switches on Luminescence in Single-Walled Nanotube Dispersions. *J. Am. Chem. Soc.* **2008**, *130*, 12734−12744.

(51) Bisker, G.; Ahn, J.; Kruss, S.; et al. A Mathematical Formulation and Solution of the CoPhMoRe Inverse Problem for Helically Wrapping Polymer Corona Phases on Cylindrical Substrates. *J. Phys. Chem. C* **2015**, *119*, 13876−13886.

(52) Jin, H.; Jeng, E. S.; Heller, D. A.; et al. Divalent Ion and Thermally Induced DNA Conformational Polymorphism on Single-walled Carbon Nanotubes. *Macromolecules* **2007**, *40*, 6731−6739.

(53) Salem, D. P.; Gong, X.; Liu, A. T.; et al. Ionic Strength-Mediated Phase Transitions of Surface-Adsorbed DNA on Single-Walled Carbon Nanotubes. *J. Am. Chem. Soc.* **2017**, *139*, 16791−16802.

(54) Gillen, A. J.; Kupis-Rozmysłowicz, J.; Gigli, C.; Schuergers, N.; Boghossian, A. A. Xeno Nucleic Acid Nanosensors for Enhanced Stability Against Ion-Induced Perturbations. *J. Phys. Chem. Lett.* **2018**, *9*, 4336−4343.

(55) Chen, K.-I.; Li, B.-R.; Chen, Y.-T. Silicon nanowire field-effect transistor-based biosensors for biomedical diagnosis and cellular recording investigation. *Nano Today* **2011**, *6*, 131−154.

(56) Ghosh, S.; Patel, N.; Chakrabarti, R. Probing the Salt Concentration Dependent Nucleobase Distribution in a Single-Stranded DNA−Single-Walled Carbon Nanotube Hybrid with Molecular Dynamics. *J. Phys. Chem. B* **2016**, *120*, 455−466.

(57) Roxbury, D.; Mittal, J.; Jagota, A. Molecular-Basis of Single-Walled Carbon Nanotube Recognition by Single-Stranded DNA. *Nano Lett.* **2012**, *12*, 1464−1469.

(58) Jana, N. R.; Gearheart, L.; Murphy, C. J. Wet Chemical Synthesis of High Aspect Ratio Cylindrical Gold Nanorods. *J. Phys. Chem. B* **2001**, *105*, 4065−4067.

(59) Ping, J.; Zhao, D.; Tianrui, C. In *The Role of Bis(p-Sulfonatophenyl)Phenylphosphine in Stabilizing Gold Nanoparticles*, Proceedings of the AASRI International Conference on Industrial Electronics and Applications; Atlantis Press, 2015; pp 44−46.

(60) Liu, X.; Atwater, M.; Wang, J.; Huo, Q. Extinction coefficient of gold nanoparticles with different sizes and different capping ligands. *Colloids Surf., B* **2007**, *58*, 3−7.

(61) Claridge, S. A.; Liang, H. W.; Basu, S. R.; Fréchet, J. M. J.; Alivisatos, A. P. Isolation of Discrete Nanoparticle−DNA Conjugates for Plasmonic Applications. *Nano Lett.* **2008**, *8*, 1202−1206.

(62) Classen, S.; Hura, G. L.; Holton, J. M.; et al. Implementation and performance of SIBYLS: a dual endstation small-angle X-ray scattering and macromolecular crystallography beamline at the Advanced Light Source. *J. Appl. Crystallogr.* **2013**, *46*, 1−13.

(63) Rosenberg, D. J.; Hura, G. L.; Hammel, M. Size Exclusion Chromatography Coupled Small Angle X-ray Scattering with Tandem Multiangle Light Scattering at the SIBYLS beamline. In *Methods in Enzymology*; Elsevier, 2022; Vol. *677*, pp 191−219.

(64) Svergun, D. I. Determination of the regularization parameter in indirect-transform methods using perceptual criteria. *J. Appl. Crystallogr.* **1992**, *25*, 495−503.

(65) Manalastas-Cantos, K.; Konarev, P. V.; Hajizadeh, N. R.; et al. *ATSAS 3.0* : expanded functionality and new tools for small-angle scattering data analysis. *J. Appl. Crystallogr.* **2021**, *54*, 343−355, DOI: 10.1107/S1600576720013412.

(66) Orthaber, D.; Bergmann, A.; Glatter, O. SAXS experiments on absolute scale with Kratky systems using water as a secondary standard. *J. Appl. Crystallogr.* **2000**, *33*, 218−225.

(67) Finnigan, J. A.; Jacobs, D. J. Light scattering by ellipsoidal particles in solution. *J. Phys. D: Appl. Phys.* **1971**, *4*, 72−77.

(68) Raval, N.; Maheshwari, R.; Kalyane, D.et al. Importance of Physicochemical Characterization of Nanoparticles in Pharmaceutical Product Development. In *Basic Fundamentals of Drug Delivery*; Elsevier, 2019; pp 369−400.

(69) Schulz, L. G. The Optical Constants of Silver, Gold, Copper, and Aluminum. I. The Absorption Coefficient k. *J. Opt. Soc. Am.* **1954**, *44*, 357−362.

(70) Schulz, L. G.; Tangherlini, F. R. Optical Constants of Silver, Gold, Copper, and Aluminum. II. The Index of Refraction n. *J. Opt. Soc. Am.* **1954**, *44*, 362−368.

(71) Manson, J.; Kumar, D.; Meenan, B. J.; Dixon, D. Polyethylene glycol functionalized gold nanoparticles: the influence of capping density on stability in various media. *Gold Bull.* **2011**, *44*, 99−105.

(72) Oesterhelt, F.; Rief, M.; Gaub, H. E. Single molecule force spectroscopy by AFM indicates helical structure of poly(ethylene-glycol) in water. *New J. Phys.* **1999**, *1*, No. 6, DOI: 10.1088/1367-2630/1/1/006.

(73) Li, M.; Jiang, S.; Simon, J.; et al. Brush Conformation of Polyethylene Glycol Determines the Stealth Effect of Nanocarriers in the Low Protein Adsorption Regime. *Nano Lett.* **2021**, *21*, 1591−1598.

(74) Cruje, C.; Chithrani, D. B. Polyethylene Glycol Functionalized Nanoparticles for Improved Cancer Treatment. *Rev. Nanosci. Nanotechnol.* **2014**, *3*, 20−30.

(75) de Gennes, P. G. Conformations of Polymers Attached to an Interface. *Macromolecules* **1980**, *13*, 1069−1075.

(76) Schindelin, J.; Arganda-Carreras, I.; Frise, E.; et al. Fiji: an open-source platform for biological-image analysis. *Nat. Methods* **2012**, *9*, 676−682.

(77) Burian, M.; Amenitsch, H. Dummy-atom modelling of stacked and helical nanostructures from solution scattering data. *IUCrJ* **2018**, *5*, 390−401, DOI: 10.1107/S2052252518005493.